INTERNATIONAL JOURNAL FOR NUMERICAL METHODS IN FLUIDS
Int. J. Numer. Meth. Fluids 2005; **47**:253–269
Published online 27 November 2004 in Wiley InterScience (www.interscience.wiley.com). DOI: 10.1002/fld.810

Calculations of 3D compressible flows using an efficient low diffusion upwind scheme

Zongjun Hu and Gecheng Zha*,†

Department of Mechanical and Aerospace Engineering, University of Miami, Coral Gables, FL 33124, U.S.A.

SUMMARY

A newly suggested E-CUSP upwind scheme is employed for the first time to calculate 3D flows of propulsion systems. The E-CUSP scheme contains the total energy in the convective vector and is fully consistent with the characteristic directions. The scheme is proved to have low diffusion and high CPU efficiency. The computed cases in this paper include a transonic nozzle with circular-to-rectangular cross-section, a transonic duct with shock wave/turbulent boundary layer interaction, and a subsonic 3D compressor cascade. The computed results agree well with the experiments. The new scheme is proved to be accurate, efficient and robust for the 3D calculations of the flows in this paper. Copyright © 2005 John Wiley & Sons, Ltd.

KEY WORDS: Riemann solver; upwind scheme; low diffusion

1. INTRODUCTION

The aircraft engine propulsion systems usually work in transonic regime, where the resolution of shock wave and boundary layer is very important. The 3D flow field calculation is usually CPU intensive. Hence, an accurate and efficient Riemann solver to resolve the shock waves and boundary layer is necessary.

The well known Roe scheme [1] is accurate to resolve the shock waves and boundary layer. However, the Roe scheme needs matrix operation for its numerical dissipation, which is fairly CPU intensive. Recently, there are many efforts to develop efficient Riemann solvers using scalar dissipation instead of the matrix dissipation. For the scalar dissipation Riemann solver schemes, there are generally two types: H-CUSP schemes and E-CUSP schemes [2–4]. The abbreviation CUSP stands for 'convective upwind and split pressure' named by Jameson [2–4]. The H-CUSP schemes have the total enthalpy from the energy equation in their convective

*Correspondence to: G. Zha, Department of Mechanical and Aerospace Engineering, University of Miami, Coral Gables, FL 33124, U.S.A.
†E-mail: zha@apollo.eng.miami.edu

Contract/grant sponsor: AFOSR; contract/grant number: F49620-03-1-0253

Received 7 March 2004
Revised 13 September 2004
Accepted 14 October 2004

vectors, while the E-CUSP schemes use the total energy in the convective vectors. The Liou's AUSM family schemes [5, 6], van Leer–Hänel scheme [7], and Edwards's LDFSS schemes [8, 9] belong to the H-CUSP group.

The H-CUSP schemes may have the advantages to better conserve the total enthalpy for steady state flows. However, from the characteristic theory point of view, the H-CUSP schemes are not fully consistent with the disturbance propagation directions, which may affect the stability and robustness of the schemes [10]. A H-CUSP scheme may have more inconsistency when it is extended to moving grid system. It will leave a pressure term multiplied by the grid velocity in the energy flux that is not contained in the total enthalpy and the term will be treated as a part of the pressure term. From characteristics point of view, it is not obvious how to treat this term in a consistent manner [11].

Recently, Zha and Hu suggested an efficient E-CUSP scheme (named as Zha CUSP) which is consistent with the characteristic directions [10]. The scheme has low diffusion and is able to capture crisp shock profiles and exact contact discontinuities. The scheme is shown to be accurate, robust and efficient. In addition, it is straightforward to extend the Zha CUSP scheme to moving grid system [11].

The original E-CUSP scheme of Zha and Hu is further modified to remove the temperature oscillations occurring occasionally near walls, in particular when the mesh is skewed. Zha modified the scheme by replacing the pressure in the dissipation of energy equation with the total enthalpy [12]. The modified scheme is named as Zha CUSP2 scheme and is tested in 2D cases in Reference [12]. The modified scheme also yields more precise wall surface temperature at coarse grid. Neither the original Zha CUSP scheme nor the Zha CUSP2 scheme has ever been applied to 3D flow field calculations.

This paper is to extend and apply the Zha CUSP2 scheme to 3D calculation of internal flows of propulsion systems. The scheme is demonstrated to be accurate, efficient, and robust for the 3D flows calculated in this paper.

2. GOVERNING EQUATIONS

The governing equations are the 3D Reynolds averaged Navier–Stokes equations in conservation law form and in generalized co-ordinates, and are given as

$$\frac{\partial \mathbf{Q}}{\partial t} + \frac{\partial \mathbf{E}}{\partial \xi} + \frac{\partial \mathbf{F}}{\partial \eta} + \frac{\partial \mathbf{G}}{\partial \zeta} = \frac{1}{Re}\left(\frac{\partial \mathbf{R}}{\partial \xi} + \frac{\partial \mathbf{S}}{\partial \eta} + \frac{\partial \mathbf{T}}{\partial \zeta}\right) \tag{1}$$

where $\mathbf{Q}$ is the conservative variable vector, $\mathbf{E}$, $\mathbf{F}$, $\mathbf{G}$ and $\mathbf{R}$, $\mathbf{S}$, $\mathbf{T}$ are the inviscid and viscous flux vectors in ξ, η, ζ directions, respectively.

To save space, only the contents of $\mathbf{Q}$, and fluxes in ξ direction, $\mathbf{E}$ and $\mathbf{R}$, are given below.

$$\mathbf{Q} = \frac{1}{J}\begin{pmatrix} \rho \\ \rho u \\ \rho v \\ \rho w \\ \rho e \end{pmatrix} \tag{2}$$

$$\mathbf{E} = \begin{pmatrix} \rho U \\ \rho u U + l_x p \\ \rho v U + l_y p \\ \rho w U + l_z p \\ (\rho e + p) U \end{pmatrix} \tag{3}$$

$$\mathbf{R} = \begin{pmatrix} 0 \\ l_x \tau_{xx} + l_y \tau_{xy} + l_z \tau_{xz} \\ l_x \tau_{xy} + l_y \tau_{yy} + l_z \tau_{yz} \\ l_x \tau_{xz} + l_y \tau_{yz} + l_z \tau_{zz} \\ l_x \beta_x + l_y \beta_y + l_z \beta_z \end{pmatrix} \tag{4}$$

where J is the transformation Jacobian, ρ is the density, e is the total energy per unit mass, u, v, w are the velocity components in x, y, z direction. The static pressure p is determined as

$$p = (\gamma - 1)\left[\rho e - \frac{1}{2}\rho(u^2 + v^2 + w^2)\right] \tag{5}$$

U is the normal contravariant velocity in generalized ξ direction,

$$U = \mathbf{V} \cdot \mathbf{l} = u l_x + v l_y + w l_z \tag{6}$$

The vector $\mathbf{l}$ is the control volume interface area vector pointing in the direction normal to the interface with its magnitude equal to the interface area. When $\Delta\xi = \Delta\eta = \Delta\zeta = 1$, $\mathbf{l}$ is expressed as the following:

$$\mathbf{l} = l_x \mathbf{i} + l_y \mathbf{j} + l_z \mathbf{k} = \frac{1}{J}(\xi_x \mathbf{i} + \xi_y \mathbf{j} + \xi_z \mathbf{k}) \tag{7}$$

Shear stress components, τ_{xx}, τ_{xy}, τ_{xz}, τ_{yy}, τ_{yz}, τ_{zz} are defined as

$$\tau_{ij} = -\frac{2}{3}(\mu + \mu_t)\frac{\partial u_k}{\partial x_k}\delta_{ij} + (\mu + \mu_t)\left(\frac{\partial u_i}{\partial x_j} + \frac{\partial u_j}{\partial x_i}\right) \tag{8}$$

where μ is the molecular viscosity, μ_t is the turbulent viscosity.

β_x, β_y, β_z are defined as

$$\beta_i = u_j \tau_{ij} - q_i \tag{9}$$

where q_x, q_y, q_z are the heat fluxes in x, y, z direction.

$$q_i = -\left[\frac{\mu}{(\gamma - 1)Pr} + \frac{\mu_t}{(\gamma - 1)Pr_t}\right]\frac{\partial a^2}{\partial x_i} \tag{10}$$

where Pr and Pr_t are the molecular and turbulent Prandtl numbers taking the value of 0.72 and 0.9. The turbulent viscosity is calculated using the Baldwin–Lomax turbulence model [13]. a is the speed of sound.

The control volume method is used to discretize the governing equations on mesh cell (i, j, k) as

$$\frac{\partial}{\partial t}\int_{\mathrm{d}V_{i,j,k}} \mathbf{Q}\,\mathrm{d}\xi\,\mathrm{d}\eta\,\mathrm{d}\zeta + (\mathbf{E}_{i+(1/2)} - \mathbf{E}_{i-(1/2)}) + (\mathbf{F}_{j+(1/2)} - \mathbf{F}_{j-(1/2)}) + (\mathbf{G}_{k+(1/2)} - \mathbf{G}_{k-(1/2)})$$
$$= \frac{1}{Re}[(\mathbf{R}_{i+(1/2)} - \mathbf{R}_{i-(1/2)}) + (\mathbf{S}_{j+(1/2)} - \mathbf{S}_{j-(1/2)}) + (\mathbf{T}_{k+(1/2)} - \mathbf{T}_{k-(1/2)})] \tag{11}$$

where $i \pm (1/2)$, $j \pm (1/2)$ and $k \pm (1/2)$ represent the control volume left and right interface locations in ξ, η and ζ directions.

3. THE E-CUSP SCHEME (ZHA CUSP2)

Take ξ direction as example, the original Zha CUSP scheme splits the inviscid flux $\mathbf{E}$ on interface $i \pm (1/2)$ into convective vector $\mathbf{E}^c$ and wave vector $\mathbf{E}^p$ to represent the velocity and pressure wave characteristics [10]. The total energy is included in the convective vector. In subsonic regime, the convective vector $\mathbf{E}^c$ is treated in an upwind manner, and the pressure vector $\mathbf{E}^p$ is averaged with the weight of the eigenvalues $U \pm C$ from both the upwind and the downwind directions. C is the speed of sound multiplied by the interface area:

$$C = a\sqrt{l_x^2 + l_y^2 + l_z^2} \tag{12}$$

where $a = \sqrt{\gamma RT}$ is the speed of sound.
The interface flux $\mathbf{E}_{(1/2)}$ is evaluated as the following:

1. In subsonic regime, $|U|_{(1/2)} < C_{(1/2)}$,

$$\mathbf{E}_{(1/2)} = \frac{1}{2}[(\rho U)_{(1/2)}(\mathbf{q}_{\mathrm{L}}^c + \mathbf{q}_{\mathrm{R}}^c) - |\rho U|_{(1/2)}(\mathbf{q}_{\mathrm{R}}^c - \mathbf{q}_{\mathrm{L}}^c)] + \begin{pmatrix} 0 \\ \mathscr{P}^+ pl_x \\ \mathscr{P}^+ pl_y \\ \mathscr{P}^+ pl_z \\ (1/2)\,p[U + C_{(1/2)}] \end{pmatrix}_{\mathrm{L}} + \begin{pmatrix} 0 \\ \mathscr{P}^- pl_x \\ \mathscr{P}^- pl_y \\ \mathscr{P}^- pl_z \\ (1/2)\,p[U - C_{(1/2)}] \end{pmatrix}_{\mathrm{R}} \tag{13}$$

where

$$\mathbf{q}^c = \begin{pmatrix} 1 \\ u \\ v \\ w \\ e \end{pmatrix} \tag{14}$$

The subscripts L and R represent the left- and right-hand sides of the interface. The interface speed of sound $C_{(1/2)}$ is computed as

$$C_{(1/2)} = \frac{1}{2}(C_{\mathrm{L}} + C_{\mathrm{R}}) \tag{15}$$

where C_{L} and C_{R} are the speed of sound determined from the left and the right side of the interface.
The mass flux on the interface is introduced as the following:

$$(\rho U)_{(1/2)} = (\rho_{\mathrm{L}} U_{\mathrm{L}}^{+} + \rho_{\mathrm{R}} U_{\mathrm{R}}^{-}) \tag{16}$$

where

$$U_{\mathrm{L}}^{+} = C_{(1/2)} \left\{ \frac{M_{\mathrm{L}} + |M_{\mathrm{L}}|}{2} + \alpha_{\mathrm{L}} \left[\frac{1}{4}(M_{\mathrm{L}} + 1)^2 - \left(\frac{M_{\mathrm{L}} + |M_{\mathrm{L}}|}{2} \right) \right] \right\} \tag{17}$$

$$U_{\mathrm{R}}^{-} = C_{(1/2)} \left\{ \frac{M_{\mathrm{R}} - |M_{\mathrm{R}}|}{2} + \alpha_{\mathrm{R}} \left[-\frac{1}{4}(M_{\mathrm{R}} - 1)^2 - \left(\frac{M_{\mathrm{R}} - |M_{\mathrm{R}}|}{2} \right) \right] \right\} \tag{18}$$

$$\alpha_{\mathrm{L}} = \frac{2(p/\rho)_{\mathrm{L}}}{(p/\rho)_{\mathrm{L}} + (p/\rho)_{\mathrm{R}}} \tag{19}$$

$$\alpha_{\mathrm{R}} = \frac{2(p/\rho)_{\mathrm{R}}}{(p/\rho)_{\mathrm{L}} + (p/\rho)_{\mathrm{R}}} \tag{20}$$

$$M_{\mathrm{L}} = \frac{U_{\mathrm{L}}}{C_{(1/2)}} \tag{21}$$

$$M_{\mathrm{R}} = \frac{U_{\mathrm{R}}}{C_{(1/2)}} \tag{22}$$

The coefficient $\mathscr{P}$ is defined as

$$\mathscr{P}_{\mathrm{L}}^{+} = \frac{1}{4}(M_{\mathrm{L}} + 1)^2(2 - M_{\mathrm{L}}) + \alpha M_{\mathrm{L}}(M_{\mathrm{L}}^2 - 1)^2 \tag{23}$$

$$\mathscr{P}_{\mathrm{R}}^{-} = \frac{1}{4}(M_{\mathrm{R}} - 1)^2(2 + M_{\mathrm{R}}) - \alpha M_{\mathrm{R}}(M_{\mathrm{R}}^2 - 1)^2 \tag{24}$$

where

$$\alpha = \frac{3}{16}$$

2. In supersonic regime, $|U|_{(1/2)} \geqslant C_{(1/2)}$, $\mathbf{E}_{(1/2)}$ is simply computed using upwind variables. When $U_{(1/2)} \geqslant C_{(1/2)}$,

$$\mathbf{E}_{(1/2)} = \mathbf{E}_{\mathrm{L}} \tag{25}$$

When $U_{(1/2)} \leqslant -C_{(1/2)}$,

$$\mathbf{E}_{(1/2)} = \mathbf{E}_{\mathrm{R}} \tag{26}$$

The above formulations are for the original Zha CUSP scheme, which can capture sharp shock profiles and exact contact surface with low diffusion [10]. However, the scheme is found to have temperature oscillations near the wall when the grid is skewed. The Zha CUSP scheme is hence modified to the following Zha CUSP2 scheme [12]:

The total enthalpy instead of the static pressure is used to compute the numerical dissipation coefficients α_{L} and α_{R} for the energy equation,

$$\alpha_{\mathrm{L}} = \frac{2(H/\rho)_{\mathrm{L}}}{(H/\rho)_{\mathrm{L}} + (H/\rho)_{\mathrm{R}}} \tag{27}$$

$$\alpha_{\mathrm{R}} = \frac{2(H/\rho)_{\mathrm{R}}}{(H/\rho)_{\mathrm{L}} + (H/\rho)_{\mathrm{R}}} \tag{28}$$

The total enthalpy is calculated as

$$H = e + \frac{p}{\rho} \tag{29}$$

It needs to emphasize that, when computing the fluxes of continuity and momentum equations, the formulations of the α_{L} and α_{R} given in Equations (19) and (20) must be used. Equations (27) and (28) are only for the energy equation.

The temperature oscillations are removed by using Equations (27) and (28) and the wall temperature is more precisely predicted by this modified scheme if a coarse grid is used [12]. This modified scheme is used for the computations in this paper.

4. TURBULENCE MODEL

To achieve high CPU efficiency, the Baldwin–Lomax turbulence model is employed in this paper for its simplicity and robustness. The Baldwin–Lomax model has been successfully applied to many 2D and 3D subsonic, transonic steady and unsteady computations [14–17]. The numerical results compare well with the experiment measurement.

The classic algebraic Baldwin–Lomax two-layer model [13] is applied to compute the turbulent viscosity μ_{t}.

At the inner layer,

$$\mu_{\mathrm{ti}} = \rho l^2 |\omega| \tag{30}$$

where

$$l = ky\left[1 - \exp\left(-\frac{y^+}{A^+}\right)\right] \tag{31}$$

ω is the local vorticity, y and y^+ are the dimensional and dimensionless distance to the wall.

At the outer layer,

$$\mu_{to} = KC_{cp}\rho F_{wake}F_{kleb} \tag{32}$$

$$F_{wake} = \min\left(y_{max}F_{max},\ C_{wake}y_{max}u_{diff}^2/F_{max}\right)$$

$$F_{kleb} = \left[1 + 5.5\left(\frac{C_{kleb}y}{y_{max}}\right)^6\right]^{-1}$$

In the above formulations, constants take the following values, $k = 0.4$, $A^+ = 26$, $C_{wake} = 0.25$, $C_{kleb} = 0.3$, $C_{cp} = 1.6$ and $K = 0.0168$.

The quantities u_{diff}, F_{max} and y_{max} are determined by the velocity profile following a line normal to the wall. F_{max} and y_{max} are the maximum value and the corresponding distance of function F_y,

$$F_y = y|\omega|\left[1 - \exp\left(-\frac{y^+}{A^+}\right)\right] \tag{33}$$

$$u_{diff} = \left(\sqrt{u^2 + v^2 + w^2}\right)_{max} - \left(\sqrt{u^2 + v^2 + w^2}\right)_{min} \tag{34}$$

In the 3D computation of this paper, there are more than one walls on the surfaces of the computation domain. At each grid point, the turbulent viscosity μ_t is first computed relative to each wall, respectively, using the above method. Then the distances to each wall are compared and the viscosity value based on the closest wall is chosen for the viscosity on the grid point. This method is applied in both the interior region and the corner regions of the computation domain. In the wake region, the exponential part is set to zero in Equations (31) and (33). The second part of Equation (34) is set to be zero outside of the wake region.

5. TIME MARCHING METHOD

The linearized governing equation, Equation (11), is solved implicitly using the line *Gauss–Seidel* iteration method. The iteration is swept line by line in the vertical η direction within each time step. The updated variables are used immediately in the previous neighbouring line during the sweep as the Gauss–Seidel iteration requires. Two alternating direction sweeps are used in each time step with one sweep from *inlet* to *outlet*, and the other from *outlet* to *inlet*. The first-order Euler scheme is used to discretize the temporal term. The first-order scheme discretization in space is also used for the implicit left-hand side operator to enhance the diagonal dominance. The accuracy of the solution is controlled by the right-hand side (RHS) of the discretized equations which use the third-order MUSCL scheme with Minmod limitor and the second-order central differencing for the viscous terms.

The discretized implicit equations are given as the following:

$$I\Delta\mathbf{Q}_{i,j,k} + A^+\Delta\mathbf{Q}_{i+1,j,k} + A\Delta\mathbf{Q}_{i,j,k} + A^-\Delta\mathbf{Q}_{i-1,j,k} + B^+\Delta\mathbf{Q}_{i,j+1,k}$$
$$+ B\Delta\mathbf{Q}_{i,j,k} + B^-\Delta\mathbf{Q}_{i,j-1,k} + C^+\Delta\mathbf{Q}_{i,j,k+1} + C\Delta\mathbf{Q}_{i,j,k} + C^-\Delta\mathbf{Q}_{i,j,k-1} = \mathbf{RHS} \tag{35}$$

where

$$\Delta\mathbf{Q} = \mathbf{Q}^{n+1} - \mathbf{Q}^n$$

$$\mathbf{RHS} = \frac{\Delta t}{\Delta V}\left\{\frac{1}{Re}[(\mathbf{R}_{i+(1/2)} - \mathbf{R}_{i-(1/2)}) + (\mathbf{S}_{j+(1/2)} - \mathbf{S}_{j-(1/2)}) + (\mathbf{T}_{k+(1/2)} - \mathbf{T}_{k-(1/2)})]\right.$$
$$\left. - [(\mathbf{E}_{i+(1/2)} - \mathbf{E}_{i-(1/2)}) + (\mathbf{F}_{j+(1/2)} - \mathbf{F}_{j-(1/2)}) + (\mathbf{G}_{k+(1/2)} - \mathbf{G}_{k-(1/2)})]\right\}^n \tag{36}$$

The superscripts n and $n+1$ denote two sequential time steps. A, B, C, A^+, B^+, C^+, A^-, B^-, C^- are derived Jacobian coefficient matrices. I is the identity matrix of order 5. The van Leer scheme [18] is used to construct the implicit Jacobians for its diagonal dominance nature.

The equation system is rewritten into the following form for η-direction line *Gauss–Seidel* iteration:

$$B^-\Delta\mathbf{U}_{i,j-1,k} + \bar{B}\Delta\mathbf{U}_{i,j,k} + B^+\Delta\mathbf{U}_{i,j+1,k} = \mathbf{RHS}^* \tag{37}$$

where

$$\bar{B} = I + A + B + C \tag{38}$$

$$\mathbf{RHS}^* = \mathbf{RHS} - A^+\Delta\mathbf{U}_{i+1,j,k} - A^-\Delta\mathbf{U}_{i-1,j,k} - C^+\Delta\mathbf{U}_{i,j,k+1} - C^-\Delta\mathbf{U}_{i,j,k-1} \tag{39}$$

6. RESULTS AND DISCUSSION

The 3D Zha CUSP2 scheme is applied to the following cases: (1) a transonic nozzle with circular-to-rectangular cross-section; (2) a transonic channel flow with shock wave/turbulent boundary layer interaction; and (3) a subsonic compressor cascade. The meshes are clustered in regions close to the wall, and the y^+ on the first inner cell center is kept less than 3 on wall boundaries for all cases. Local time stepping is used to speed up the convergence.

6.1. Turbulence model validation

The accuracy of the *Baldwin–Lomax* turbulence model is validated with computing a flat plate turbulent boundary layer flow. The mesh is distributed as 80 points uniformly allocated along the wall surface and 60 points allocated normal to the wall surface with a stretch factor of 1.1. The y^+ of the first cell centre to the wall is kept under 0.2. The Reynolds number based on the plate length is 4×10^6. The inlet Mach number is 0.5. When applying the line Gauss–Seidel relaxation method, the CFL number is set to be 100. The computed result is compared very well with the law of the wall as shown in Figure 1.

6.2. Circular-to-rectangular nozzle

A transonic nozzle with circular-to-rectangular cross-section tested at NASA [19] is calculated. The transition duct connects the axisymmetric engine to the non-axisymmetric nozzle

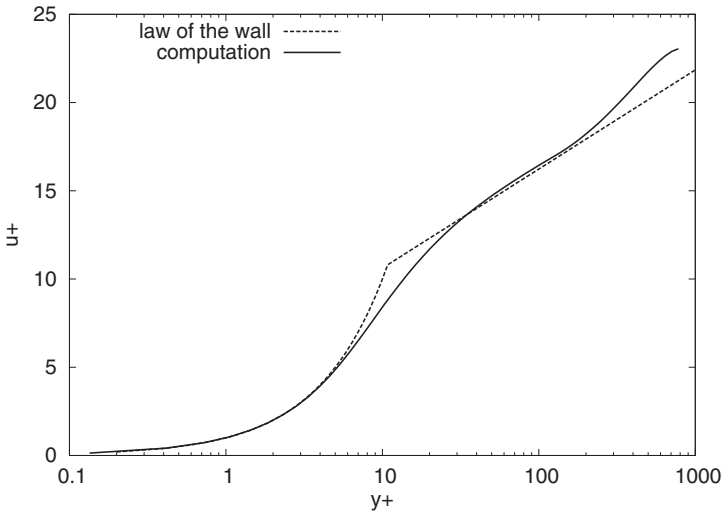

Figure 1. Computed turbulent boundary layer velocity profile compared with the law of the wall.

through a smooth progression of geometrically similar cross-sections. There is no swirl flow at the inlet. The Reynolds number based on the inlet diameter is $Re = 7.7058 \times 10^5$. Due to its symmetric structure, only a quarter of the nozzle geometry is computed as shown in Figure 2. Two symmetric boundaries are located at the bottom and back sides. The wall is divided into two parts to generate the H-type mesh. For clarity, every two other grid line is omitted in each direction in the plot. The baseline mesh size is $100 \times 50 \times 50$ and is highly stretched near the walls. No shock wave exists in the flow field. The total pressure, total temperature and flow angles are fixed at the inlet as the boundary conditions. Because of the supersonic flow at the outlet, the zero-gradient boundary condition is used at the nozzle exit. No slip and adiabatic wall conditions are used for the walls. The optimum CFL number used is 200.

Figure 3 shows the contour lines of Mach number on the bottom symmetric plane for Zha CUSP2 scheme. The flow accelerates from subsonic at the inlet, reaches sonic at the nozzle throat, and becomes supersonic at the exit. The top wall and side wall static pressure distributions are compared with experimental results in Figures 4 and 5, respectively. Good agreement is obtained.

Because Zha CUSP2 scheme uses scalar dissipation and hence is more CPU efficient than the Roe scheme. On an Intel Xeon 1.7G Hz processor, the CPU time used to compute the inviscid flux per step per node is 1.84×10^{-5} s for the Zha CUSP2 scheme and 2.9723×10^{-5} s for the Roe scheme. The Zha CUSP2 scheme is about 40% more efficient.

Mesh refinement study is carried out by doubling mesh density in ξ, η and ζ directions, respectively. The computation results with mesh size $200 \times 50 \times 50$, $100 \times 100 \times 50$ and $100 \times 50 \times 100$ are also plotted in Figures 4 and 5. The same height is kept on the first inner cell close to the wall boundary for the mesh refinement. The mesh refinement gives about the same results as the original baseline mesh as shown in Figures 4 and 5, which indicate that the solution is converged based on the mesh refinement.

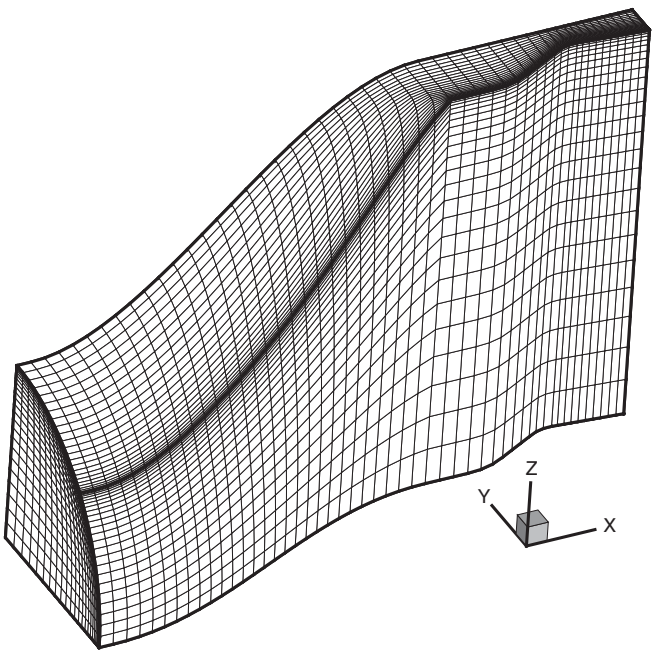

Figure 2. The mesh of the nozzle with circular-to-rectangular cross-section.

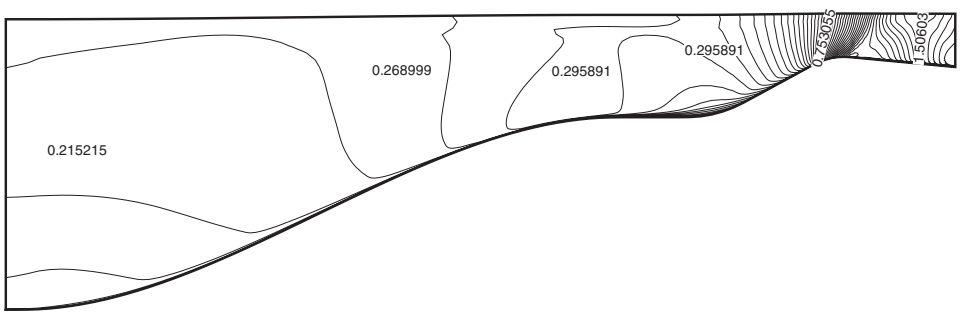

Figure 3. Mach number contours of the nozzle with circular-to-rectangular cross-section.

6.3. 3D compressor cascade

The third case is to calculate a 3D subsonic compressor cascade tested at NASA GRC [20]. The cascade has the chord length of 8.89 cm, the stagger angle of 60° and the solidity of 1.52. In the experiment, the geometry incidence is set to 0°. However, due to the side wall boundary layer effect, the actual incidence angle is considered to be 1–1.5° higher. In the numerical simulation, the incidence angle is set as 1.5°. The Reynolds number based the chord length is 9.67×10^5. A mesh of $100 \times 60 \times 60$ is used in the computation with every other mesh line omitted (Figure 6).

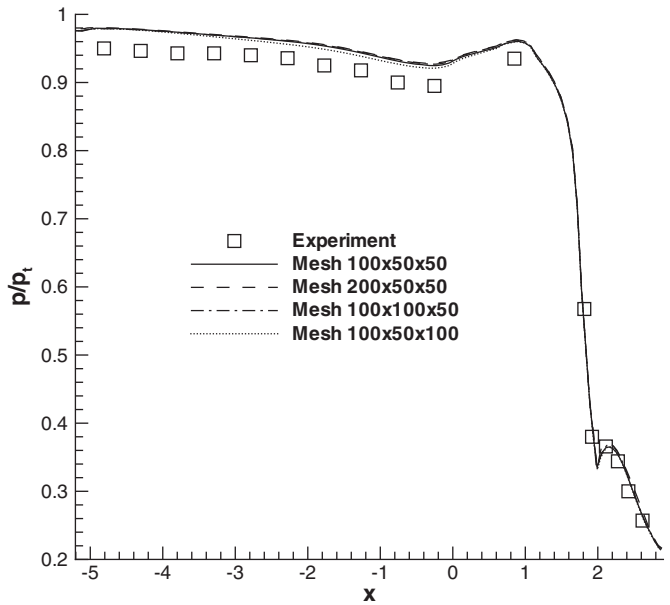

Figure 4. Top wall surface pressure distributions of the nozzle with circular-to-rectangular cross-section compared with the experiment [19].

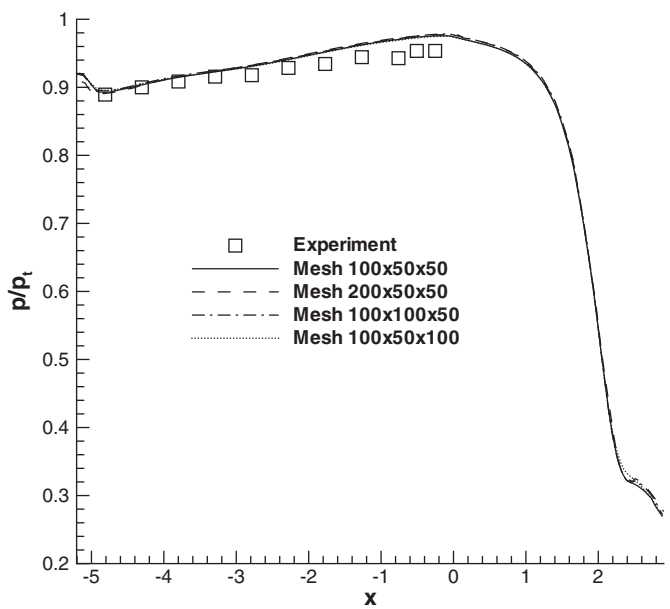

Figure 5. Side wall surface pressure distributions of the nozzle with circular-to-rectangular cross-section compared with the experiment [19].

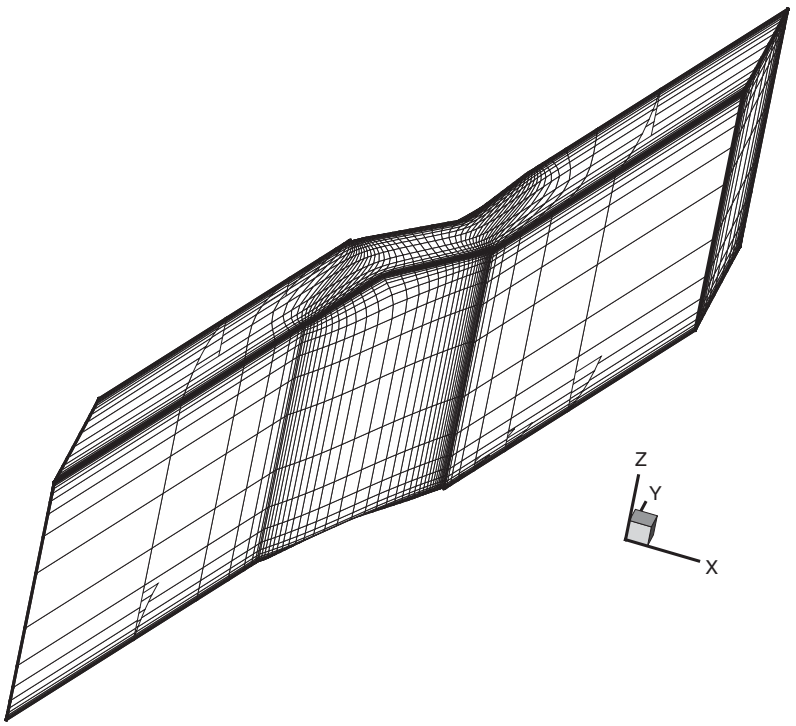

Figure 6. 3D cascade mesh.

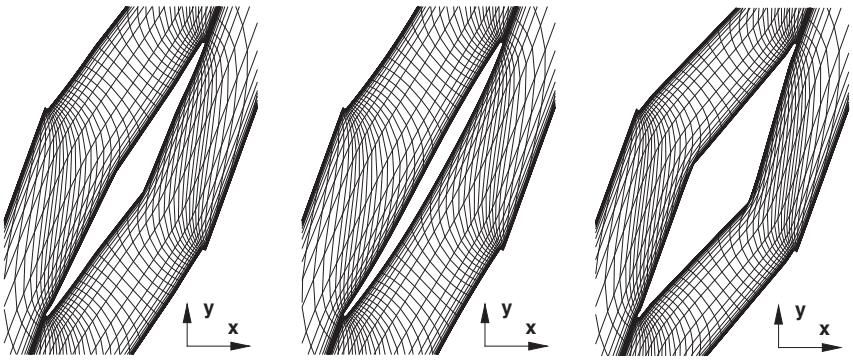

Figure 7. Cascade mesh on the bottom plane (left), mid-span plane (middle), and top plane (right).

The simulation includes the top and bottom end walls, where the cascade airfoil shape is very different from the one at the midspan as shown in Figure 7. The computation starts from zero initial velocity field. The total pressure, total temperature and flow angles are fixed at the inlet. The static pressure is specified at the outlet. No slip and adiabatic wall boundary condi-

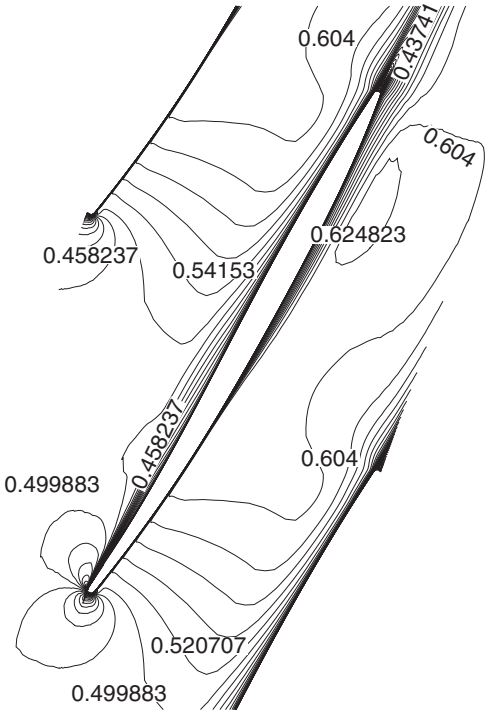

Figure 8. Cascade Mach contours on the mid-span plane.

tions are applied on blade surfaces, top and bottom end walls. Periodic boundary conditions are applied upstream and downstream of the blade in pitch direction.

Figure 8 shows the Mach number contours of Zha CUSP2 scheme on the mid-span plane. Figure 9 shows that the computed surface pressure ($C_p = (p_\infty - p)/\rho_\infty U_\infty^2$) distribution agrees very well with the experiment. The result of the Zha CUSP2 scheme is also virtually identical to that of the Roe scheme.

6.4. Transonic channel flow

The last case is a transonic channel flow with shock wave/turbulent boundary–layer interaction and is studied experimentally in Reference [21]. The test section of the transonic channel has an entrance height of 100 mm and a width of 120 mm. It is composed of a straight top wall, two straight side walls. A bump with varying shape in span-wise direction is mounted on the bottom wall. The boundary conditions use fixed total pressure, total temperature and flow angles at the inlet and fixed static pressure at the outlet. No slip adiabatic wall boundary conditions are used on the walls.

In the present computation, the inlet Mach number is about 0.5. The Reynolds number based on the entrance height is 5×10^5. A mesh of $90 \times 60 \times 60$ is used for computation. The mesh is mostly uniformly distributed in the horizontal direction, but clustered in the bump region to better resolve the shock wave. Figure 10 shows the 3D mesh with every two other

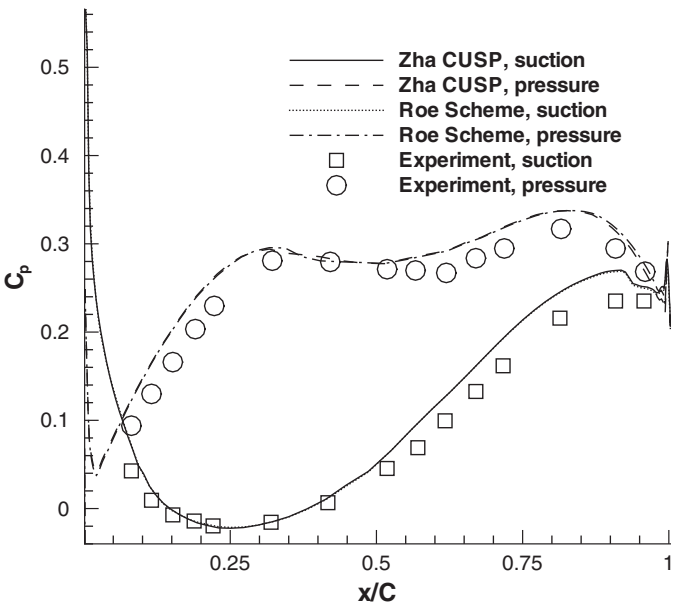

Figure 9. Cascade mid-span plane surface pressure coefficient distributions compared with experiment measurement [20].

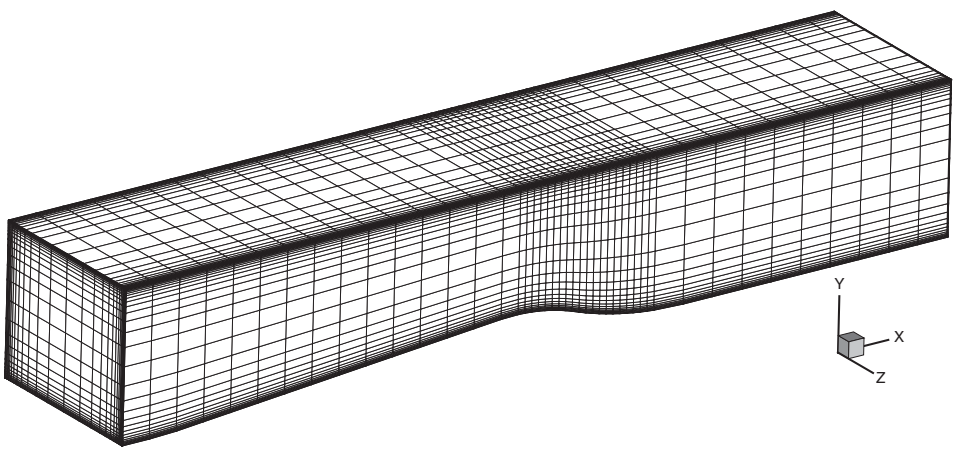

Figure 10. Transonic duct mesh.

grid line omitted for clarity. To resolve the turbulent boundary layer, the mesh is clustered near the four walls.

Figure 11 shows the computed shock wave structure (Mach number contour) compared with the experiment [22] at three spanwise planes. They are located at $Z = 60$, 75 and 90 mm away from the back wall, respectively. The plane at 60 mm is the central plane of the channel. The outlet static pressure is adjusted to achieve the same shock location as that in the experiment.

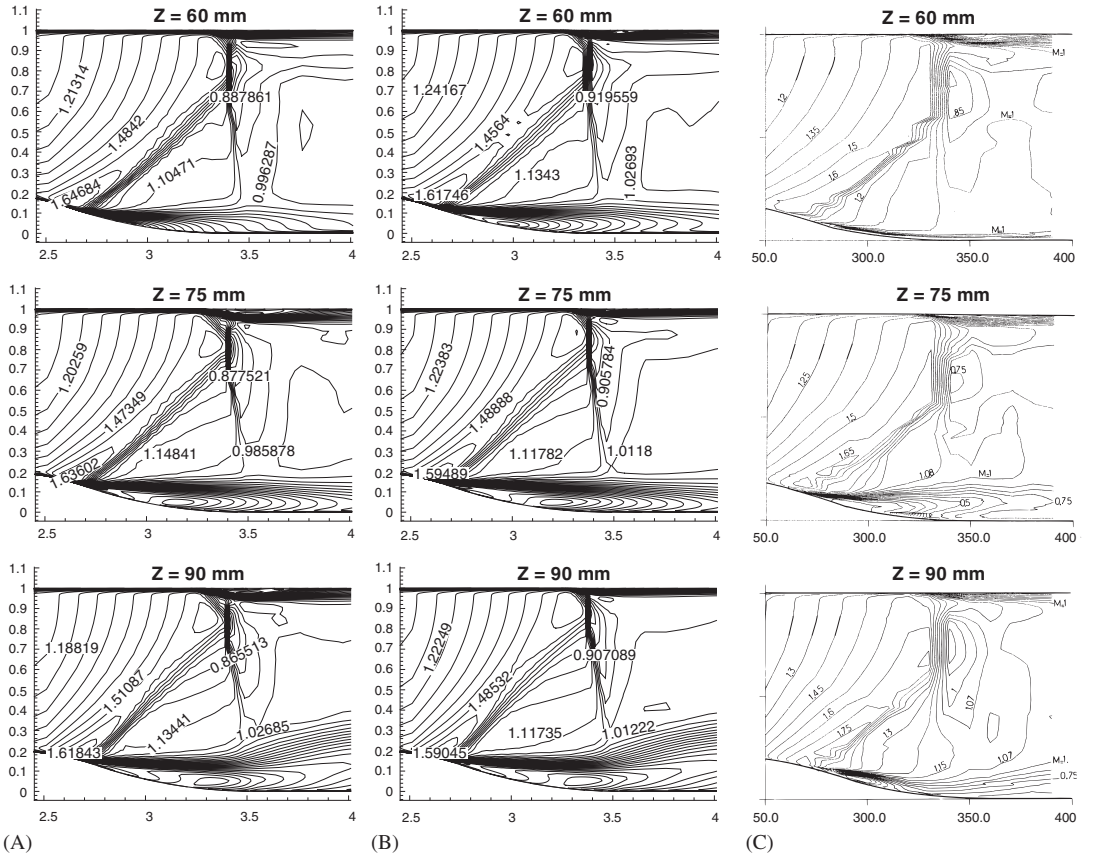

Figure 11. Transonic duct Mach number contours: (A) Zha CUSP2 scheme; (B) Roe scheme; and (C) experiment.

The back pressure has the value of $p_{\text{outlet}}/p_{\text{t}} = 0.53$. The Zha CUSP2 scheme and the Roe scheme result in the shock wave structure very similar to the experiment. The computed maximum Mach numbers using Roe and Zha CUSP2 scheme are a little lower than that in the experiment. However, the Zha CUSP2 scheme gives the maximum Mach number closer to the experiment than the Roe scheme. Both the schemes predict the boundary layer thicker than that measured in the experiment. This may be mainly due to the inadequacy of the turbulence modeling. The Baldwin–Lomax model is based on the empirical mixing length assumption and is more reliable for attached flows in equilibrium [23]. In the transonic channel, the flow is separated after the throat, which makes the performance of the Baldwin–Lomax model not as good as the second and the third cases with flow attached.

At $Z = 60$ mm, the experiment shows no flow separation, so does the Zha CUSP2 scheme. However, the Roe scheme predicts a flow separation at that location. At location $Z = 75$ mm, both the Zha CUSP2 scheme and the Roe scheme predict the flow separation similar to the experiment. However, at the location $Z = 90$ mm which is close to the side wall, the results computed by both the schemes predict larger separation zone than that of the experiment.

The mesh refinement study with the mesh size of $180 \times 60 \times 60$, $90 \times 90 \times 60$ and $90 \times 60 \times 90$ gives very similar results, which indicates that the solution is mesh independent.

7. CONCLUSION

The newly suggested E-CUSP upwind scheme with scalar dissipation, Zha CUSP2 scheme, is applied for the first time to calculate the 3D flows for propulsion systems.

For the transonic nozzle with circular-to-rectangular cross-section and the subsonic compressor cascade, the wall static pressure distributions computed by the Zha CUSP2 scheme are in good agreement with the experiments. The CPU time to calculate the flux using the Zha CUSP2 scheme is about 40% more efficient than that used by the Roe scheme.

For the transonic channel case, the shock wave structure given by Zha CUSP2 scheme agrees well with the experiment. The result of Zha CUSP2 scheme agrees better with the experiment than the one predicted by the Roe scheme, which gives flow separation that does not exist in the experiment. The Zha CUSP2 scheme also predicts the peak Mach number closer to the experiment than that of the Roe scheme.

The Zha CUSP2 scheme is shown to be accurate, efficient and robust for the 3D flows calculated in this paper.

ACKNOWLEDGEMENTS

This work is partially supported by AFOSR Grant F49620-03-1-0253 monitored by Dr Fariba Fahroo.

REFERENCES

1. Roe P. Approximate Riemann solvers, parameter vectors, and difference schemes. *Journal of Computational Physics* 1981; **43**:357–372.
2. Jameson A. Analysis and design of numerical schemes for gas dynamics I: artificial diffusion, upwind biasing, limiters and their effect on accuracy and multigrid convergence in transonic and hypersonic flow. *AIAA Paper 93-3359*, 7, 1993.
3. Jameson A. Analysis and design of numerical schemes for gas dynamics I: artificial diffusion, upwind biasing, limiters and their effect on accuracy and multigrid convergence in transonic and hypersonic flow. *Journal of Computational Fluid Dynamics* 1995; **4**:171–218.
4. Jameson A. Analysis and design of numerical schemes for gas dynamics II: artificial diffusion and discrete shock structure. *Journal of Computational Fluid Dynamics* 1995; **5**:1–38.
5. Liou M-S, Steffen CJ. A new flux splitting scheme. *Journal of Computational Physics* 1993; **107**:1–23.
6. Liou M-S. Ten years in the making—AUSM family. *AIAA Paper 2001-2521*, 2001.
7. Hänel D, Schwane R, Seider G. On the accuracy of upwind schemes for the solution of the Navier–Stokes equations. *AIAA Paper 87-1105 CP*, 1987.
8. Edwards JR. A low-diffusion flux-splitting scheme for Navier–Stokes calculations. *AIAA Paper 95-1703-CP*, 6, 1995.
9. Edwards JR. A low-diffusion flux-splitting scheme for Navier–Stokes calculations. *Computer and Fluids* 1997; **6**:635–659.
10. Zha G-C, Hu Z-J. Calculation of transonic internal flows using an efficient high resolution upwind scheme. *AIAA Journal* 2004; **42**(2):205–214.
11. Xiangying Chen, Gecheng Zha. Fully coupled fluid–structural interactions using an efficient high resolution upwind scheme. *AIAA Paper 2004-2331*, 2004.
12. Gecheng Zha. A low diffusion efficient E-CUSP upwind scheme for transonic flows. *AIAA Paper 2004-2707*, *34th AIAA Fluid Dynamics Conference*, 28 June–1 July 2004.
13. Baldwin BS, Lomax H. Thin layer approximation and algebraic model for separated turbulent flows. *AIAA Paper 78-257*, 1978.

14. Baysal O, Hoffman WB. Simulation of three-dimensional shear flow around a nozzle-afterbody at high speeds. *Journal of Fluids Engineering* 1992; **114**:178–185.
15. Chen JP, Whitfield DL. Navier–Stokes calculations for the unsteady flowfield of turbomachinery. *AIAA Paper 93-0676*, 1993.
16. Grüber B, Carstens V. The impact of viscous effects on the aerodynamic damping of vibrating transonic compressor blades—a numerical study. *Journal of Turbomachinery* 2001; **123**:409–417.
17. Weber S, Platzer MF. A Navier–Stokes analysis of the stall flutter characteristics of the Buffum cascade. *Journal of Turbomachinery* 2000; **122**:769–776.
18. van Leer B. *Flux-vector Splitting for the Euler Equations*, Lecture Note in Physics vol. 170, 1982; 507–512.
19. Burley II JR, Bangert LS, Carlson JR. Static investigation of circular-to-rectangular transition ducts for high-aspect-ratio nonaxisymmetric nozzles. *NASA Technical Paper 2534*, 1986.
20. Buffum DH, Capece VR, King AJ, EL-Aini YM. Oscillating cascade aerodynamics at large mean incidence. *Technical Memorandum 107247*, NASA, 1996.
21. Délery JM. Experimental investigation of turbulence properties in transonic shock/boundary–layer interaction. *AIAA Journal* 1983; **21**:180–185.
22. Benay R, Délery J, Pot T. Etude expérimentale d'une interaction onde de choc-couche limite en canal tridemensionnel. Propriétś du champ moyen. *Rapport Technique No. 70/7078 AN*, ONERA, 1986.
23. Gacherieu C, Weber C. Assessment of algebraic and one-equation turbulence models for the transonic turbulent flow around a full aircraft configuration. *AIAA Paper 98-2737*, 1998.

